Unusual quantum effects in scattering wavefunctions of two-dimensional cage potentials

2005 J. Phys. A: Math. Gen. 38 9821

(http://iopscience.iop.org/0305-4470/38/45/007)

INSTITUTE OF PHYSICS PUBLISHING JOURNAL OF PHYSICS A: MATHEMATICAL AND GENERAL

J. Phys. A: Math. Gen. **38** (2005) 9821–9847 doi:10.1088/0305-4470/38/45/007

Unusual quantum effects in scattering wavefunctions of two-dimensional cage potentials

Kirk D Rowe[1] **and Philip J Siemens**

Department of Physics, Oregon State University, Corvallis, OR, USA

E-mail: kirkrowe@lifetime.oregonstate.edu

Received 28 May 2005, in final form 3 October 2005
Published 26 October 2005
Online at stacks.iop.org/JPhysA/38/9821

Abstract

We exhibit long-lived resonances in scattering from two-dimensional soft cage potentials comprised of three and four Gaussian peaks. Specific low-energy resonances with very narrow width are shown to correspond to classical multiple-reflection events. These states have much larger probability densities inside the cage than outside and mimic bound states in the sense that the symmetry-breaking effect of the incident wave is relatively small. As a result, we have found that isolated states display the simple symmetry characteristics of bound states. Overlapping resonances exhibit a mixing of symmetry classes leading to wavefunctions of lower symmetry, like those of wider resonances at higher energy. We demonstrate that at energies below the lowest resonances of two-dimensional cages, where the distance across the entrance of the cage corresponds to less than half a wavelength, the wavefunction may still gain access to the interior region by squeezing its wavelength in the necessary direction at the expense of the kinetic energy in the direction normal to the opening. The resulting curvature of the wavefunction in the donor dimension corresponds to an imaginary wave number, curving away from the plane defined by zero amplitude. This mechanism for passing between obstacles may be relevant for electronic and optical devices having spatial structures with dimensions comparable to the wavelengths of the energy carriers.

PACS numbers: 03.65.Nk, 03.67.Lx

1. Introduction

The importance of scattering and resonant features in contemporary physics cannot be overlooked. The realization of Moore's law over the last four decades, for example, has stimulated a growing interest in the area of mesoscopic physics, specifically in the field of

[1] Present address: 756 Elm Street, Glen Ellyn, IL 60137, USA.

nano and molecular electronics. Aggressive miniaturization of electronic components requires a detailed understanding of the quantum effects that govern them. These devices are based on the quantum properties of electrons, moving in up to three dimensions, confined to an island or a region separated from both the source and the drain by a potential barrier [1]. Such systems include quantum dots, resonant tunnelling devices and single-electron transistors. Current flow through them is intimately tied to their resonance structure and their quantum transport properties. As computers, in turn, gain power, it becomes possible to investigate complicated models with nonseparable potentials that require the extension of one-dimensional techniques to multiple dimensions.

One new area where this multidimensional analysis is being applied is to photonic crystal fibres (PCFs) [2], which have been manufactured for less than a decade. These are optical fibres that have a regular array of air channels along their length surrounding some central defect. This central defect may be a larger hollow central channel or, as in the case of a solid-core PCF, the absence of such a channel. For the hollow-core case, the mechanism for light propagation along the fibre is not due to total internal reflection, which requires a cladding of a relatively lower refraction index, but instead is realized through photonic band gaps or optical suppression in the direction transverse to the fibre's length. For the solid-core fibres, on the other hand, the average index of the channelled medium surrounding the solid central core is reduced, making total internal reflection possible for certain frequencies. With white light introduced at one end of the fibre, only certain colours are visible on the other end. The complex structure of PCFs dictates that Maxwell's equations must be solved numerically. This task, in the case of a two-dimensional microstructured fibre, decouples into two problems: propagation along the length of the fibre, and scattering in the transverse plane. For transverse in-plane scattering, the full vector problem may be decomposed into a scalar Helmholtz problem for each of the two principal polarizations $E_{\parallel}$ and $H_{\parallel}$ [3, 4]. Solid-core PCFs are now marketed commercially as endlessly single mode [5], not possible for conventional optic fibres. The air holes in the PCF's cross section act as a modal sieve. The fundamental mode has a transverse wavelength too long to escape through the gaps, while higher modes can leak away between the air holes. This caging effect may be tuned by adjusting the diameter of the holes, making it possible to trap additional modes. Adjusting the exact geometry may resonate the fundamental mode which in turn can affect dispersion properties. For pulsed digital communication, it is obviously advantageous to minimize packet spreading.

Exploring the foundations of this new frontier, we have made some interesting observations and uncovered an as-yet undocumented physical behaviour. In this paper, the Lippmann–Schwinger technique is applied to noncentral potentials in two dimensions. We use the theory to compute transition matrices for open quantum systems governed by repulsive soft hyperbolically defocusing scatterers that may trap quantum particles either through multiple internal reflection or by a quantum caging effect. This allows us to describe the given system in terms of its wavefunctions, resonances and cross sections. Low-lying long-lived resonances are investigated for both tri-peaked and quad-peaked repellers to determine wavefunction symmetries and other universal characteristics. One novel feature is a phenomenon similar to quantum tunnelling which allows a wavefunction to penetrate a narrow aperture less than a half wavelength wide. This is accomplished by borrowing kinetic energy from the propagation direction, which can change the sign of the curvature in that dimension, to localize the wave transversely. This squeezing in the crucial dimension is the mechanism by which the wavefunction gains passage. This phenomenon does not present itself for one-dimensional systems due to the lack of a secondary or donor dimension.

Of particular interest are results by Peskin *et al* [6] suggesting electron tunnelling enhancement by resonances in the frozen water picture. The resonances were found to

coincide with those energies, lying low in the potential, for which tunnelling was intensified by many orders of magnitude. Due to the complicated potential, however, the associated wave mechanics are difficult to analyse. The much simpler potential structure in our work allows us to see how the transmitted electron is able to negotiate its way between resonant cavities.

An exact two-dimensional quantum theory is presented in section 2 while the particulars of its specific implementation for chosen three- and four-centre scatterers are covered in section 3. Results are given in section 4, followed by conclusions which are summarized in the final section.

2. Exact quantum theory

2.1. Basic equations

For a given potential V, the scattering solutions to the time-independent Schrödinger equation,

$$(H_o + V)|\Psi\rangle = E|\Psi\rangle, \tag{1}$$

may be written in terms of a Green's function, G_E, by first introducing the unscattered wave $|\varphi_{\mathbf{k}_o}\rangle = e^{i\mathbf{k}_o\cdot\mathbf{r}}/2\pi$ as a boundary condition,

$$|\Psi_{\mathbf{k}_o}\rangle = |\varphi_{\mathbf{k}_o}\rangle + G_E V|\Psi_{\mathbf{k}_o}\rangle; \qquad G_E \equiv (E - H_o)^{-1}. \tag{2}$$

An outwardly scattered wave is imposed as the additional boundary condition by adding a small imaginary energy $i\varepsilon$ to E in (2) which defines how the integration contour is to be distorted at the poles. By introducing the transition matrix T for outward scattering, the previous equations may now be written as

$$|\Psi^+_{\mathbf{k}_o}\rangle = |\varphi_{\mathbf{k}_o}\rangle + G^+_E T|\varphi_{\mathbf{k}_o}\rangle; \qquad G^+_E \equiv (E - H_o + i\varepsilon)^{-1}, \qquad T|\varphi_{\mathbf{k}_o}\rangle = V|\Psi^+_{\mathbf{k}_o}\rangle. \tag{3}$$

To find the wavefunction we first find T by allowing the potential to operate on (2) from the left,

$$T|\varphi_{\mathbf{k}_o}\rangle = V|\varphi_{\mathbf{k}_o}\rangle + VG^+_E T|\varphi_{\mathbf{k}_o}\rangle, \tag{4}$$

yielding a solution in terms of the Møller wave operator,

$$T = \Omega V; \qquad \Omega \equiv \left(I - VG^+_E\right)^{-1}. \tag{5}$$

In terms of this new wave operator, (3) is expressible in its most concise form,

$$|\Psi^+_{\mathbf{k}_o}\rangle = \Omega|\varphi_{\mathbf{k}_o}\rangle. \tag{6}$$

For an expanded treatment, see the text on collision theory [7–9]. From the wavefunction, the current density and velocity field,

$$\mathbf{J}(\mathbf{r}) = \frac{\hbar}{2\mu i}[\Psi^*(\mathbf{r})\nabla\Psi(\mathbf{r}) - \Psi(\mathbf{r})\nabla\Psi^*(\mathbf{r})], \tag{7}$$

$$\mathbf{v}(\mathbf{r}) = \mathbf{J}(\mathbf{r})/[\Psi^*(\mathbf{r})\Psi(\mathbf{r})], \tag{8}$$

may also be calculated. As the scattering amplitudes are proportional to the transition matrix elements,

$$f_{\mathbf{k}\mathbf{k}_o} \propto T_{\mathbf{k}\mathbf{k}_o}, \tag{9}$$

solving (5) allows computation of both differential and total cross sections.

The system's resonances correspond to complex energies for which Ω is singular,

$$\left|\Omega_E^{-1}\right| = 0; \qquad E \in \mathcal{Z}. \tag{10}$$

2.2. *Representations of equations*

Operating on (4) from the left with the free-particle wavefunction in a basis of δ-function normalized momentum eigenstates, $|\mathbf{k}\rangle$, and rearranging terms, gives

$$\langle \mathbf{k}|V|\mathbf{k}_o\rangle = \langle \mathbf{k}|T|\mathbf{k}_o\rangle - \int \frac{\langle \mathbf{k}|V|\mathbf{k}'\rangle\langle \mathbf{k}'|T|\mathbf{k}_o\rangle}{E(\mathbf{k}_o) - H_o(\mathbf{k}') + i\varepsilon}\,d\mathbf{k}', \tag{11}$$

where we have used the closure identity. For a free-particle Hamiltonian,

$$H_o(\mathbf{k}) = \frac{\mathbf{p}^2}{2\mu} = \frac{\hbar^2 k^2}{2\mu}; \qquad k \equiv \sqrt{\mathbf{k}^2}, \tag{12}$$

the poles of (11) depend only on the magnitude of the momentum, k.

Specializing to two dimensions, we simplify computations by choosing a polar representation in terms of k and the scattering angle, θ. The explicit polar representation of the matrix elements of (11) is

$$V(k,\theta;k_o,\theta_o) = T(k,\theta;k_o,\theta_o) - \frac{2\mu}{\hbar^2}\int_0^{2\pi}\int_0^{\infty} \frac{V(k,\theta;k',\theta')T(k',\theta';k_o,\theta_o)}{k_o^2 - k'^2 + i\epsilon}k'\,dk'\,d\theta'. \tag{13}$$

Similarly, (3) may be projected onto a coordinate basis, $|\mathbf{r}\rangle$, to arrive at an expression for the wavefunction, $\Psi^+_{\mathbf{k}_o}(\mathbf{r}) \equiv \langle \mathbf{r} \mid \Psi^+_{\mathbf{k}_o}\rangle$,

$$\Psi^+_{\mathbf{k}_o}(\mathbf{r}) = \frac{e^{i\mathbf{k}_o\cdot\mathbf{r}}}{2\pi} + \frac{\mu}{\pi\hbar^2}\int_0^{2\pi}\int_0^{\infty} \frac{e^{i\mathbf{k}'\cdot\mathbf{r}}}{k_o^2 - k'^2 + i\epsilon}T(k',\theta';k_o,\theta_o)k'\,dk'\,d\theta'. \tag{14}$$

In two dimensions, the propagator for the Helmholtz equation is proportional to the Hankel function of the first kind and order zero [12, 13].

$$G^+_{k_o}(\mathbf{r},\mathbf{r}') = \frac{\hbar^2}{2\mu}G^+_E(\mathbf{r},\mathbf{r}') = \frac{1}{4i}H_o^{(1)}(k_o|\mathbf{r}-\mathbf{r}'|) \longrightarrow \begin{cases} \dfrac{1}{2\pi}\ln(k_o|\mathbf{r}-\mathbf{r}'|) : |\mathbf{r}-\mathbf{r}'| \to 0, \\ \dfrac{e^{i(k_o|\mathbf{r}-\mathbf{r}'|-\pi/4)}}{2i\sqrt{2\pi k_o|\mathbf{r}-\mathbf{r}'|}} : |\mathbf{r}-\mathbf{r}'| \to \infty. \end{cases} \tag{15}$$

If the asymptotic form of this propagator is applied to (14) and the result then compared to the asymptotic form of the scattered wave,

$$\lim_{r\to\infty}\Psi^+_{\mathbf{k}_o}(\mathbf{r}) = \frac{1}{2\pi}\left[e^{i\mathbf{k}_o\cdot\mathbf{r}} + \frac{f_{k_o}(\theta)\,e^{ik_o r}}{\sqrt{r}}\right], \tag{16}$$

the relationship between the scattering amplitude and the transition matrix is revealed,

$$f_{k_o}(\theta) = -\frac{2\pi\mu}{\hbar^2}\sqrt{\frac{\pi}{k_o}}(1+i)T(\mathbf{k},\mathbf{k}_o). \tag{17}$$

It follows that the differential cross section in the two-dimensional space is

$$\frac{d\lambda}{d\theta} = \left|f_{k_o}(\theta)\right|^2 = \frac{8\pi^3\mu^2}{\hbar^4 k_o}|T(\mathbf{k},\mathbf{k}_o)|^2. \tag{18}$$

Because the cross section in two dimensions has units of length, λ is used here.

3. Procedure

3.1. Numerical methods

To find discretized approximations to our equations that could be implemented on computers, we constructed a polar grid in momentum space having mesh points (k_i, θ_j) and associated weights given by w_i and ω_j. In the angular direction, we used Gauß–Legendre points distributed symmetrically about π on a full azimuthal interval of $[0, 2\pi]$ to take advantage of cancellations stemming from the differences of derivatives at interval boundaries.

The radial integrals posed two challenges, at $k' = k_o$ and $k' \to \infty$. Aside from the singularities, the local potentials we studied depend on the differences $k_x - k'_x$ and $k_y - k'_y$, requiring that these integrals be carried out to large values of k'. To regularize the poles, we employed two different methods and confirmed that their results agree.

For the scattering problem, k_o is real and we were able to remove the poles through a standard subtraction technique [14, 15]. Applying the identity

$$\lim_{\epsilon \to 0} \int_0^\infty \frac{f(k')}{k_o^2 - k'^2 + i\epsilon}\, dk' = \int_0^\infty \frac{f(k') - f(k_o)}{k_o^2 - k'^2}\, dk' - \frac{i\pi}{2k_o} f(k_o) \tag{19}$$

to (13) produces the equation

$$\begin{aligned} V(k, \theta; k_o, \theta_o) = {} & T(k, \theta; k_o, \theta_o) \\ & - \frac{2\mu}{\hbar^2} \sum_{j=1}^{m} \omega_j \sum_{i=1}^{n} w_i \frac{V(k, \theta; k'_i, \theta'_j) T(k'_i, \theta'_j; k_o, \theta_o) k'}{k_o^2 - k_i'^2} \\ & + \frac{2\mu}{\hbar^2} \sum_{j=1}^{m} \omega_j V(k, \theta; k_o, \theta_j) T(k_o, \theta_j; k_o, \theta_o) k_o \sum_{i=1}^{n} \frac{w_i}{k_o^2 - k_i'^2} \\ & + i\pi \frac{\mu}{\hbar^2} \sum_{j=1}^{m} \omega_j V(k, \theta; k_o, \theta_j) T(k_o, \theta_j; k_o, \theta_o), \end{aligned} \tag{20}$$

used to solve for the matrix elements of T. Because the subtraction technique redistributes the information held at a singularity across the entire real line, the radial integration may be sensitive to truncation, dictating our use of appropriately scaled Gauß–Legendre points in the radial direction as well. Systems of N equations were constructed by allowing (k, θ) to take on the values of each of the mesh points in addition to the on-shell momenta (k_o, θ_j). Observing the restriction $k' \neq k_o$, these resulting systems of up to $N = 7500$ (which represents the upper limit for a gigabyte of physical memory) double-precision complex equations were then solved simultaneously using the well optimized, 'canned' `LAPACK` subroutine `ZGESV` and its subroutines provided in the netlib repository (`www.netlib.org`). Subsequently, the wavefunctions, (14), were then calculated by matrix multiplication.

We tested our coding for the T-matrix calculation on an azimuthally symmetric potential which could include both attractive and repulsive regions by the choice of two parameters, V_a and V_b,

$$V(r) = \frac{[V_a r^2 - V_b]}{\exp(r^2)}. \tag{21}$$

Resulting cross sections from our code were compared with those obtained from the partial wave shifts of the angular momentum eigenfunctions in two dimensions. Agreement was established in all cases.

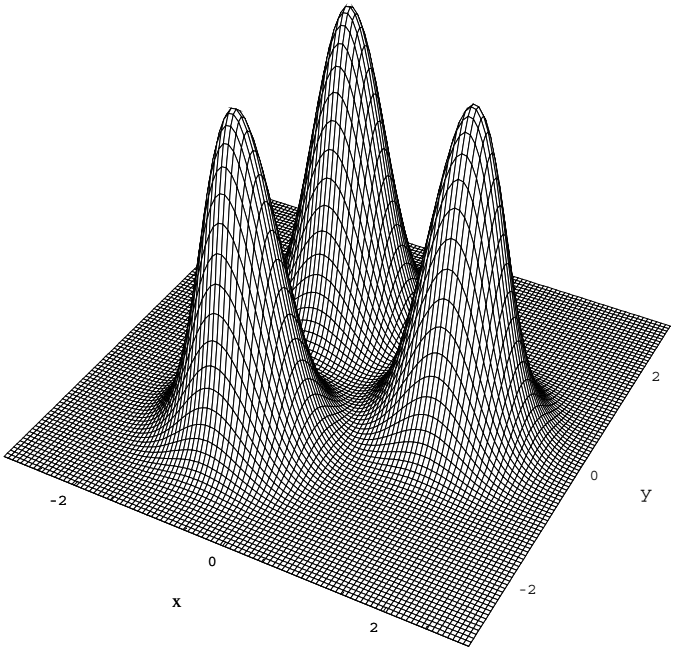

Figure 1. Three-centre scatterer.

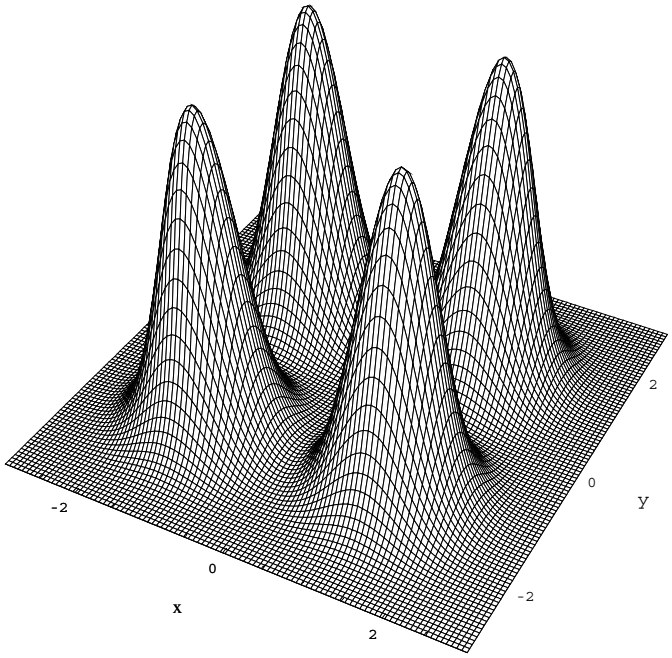

Figure 2. Four-centre scatterer.

Resonances and their widths, Γ, are defined as solutions of (10) where the energy, E, of the system is analytically continued to the fourth quadrant of the second Riemann sheet of the

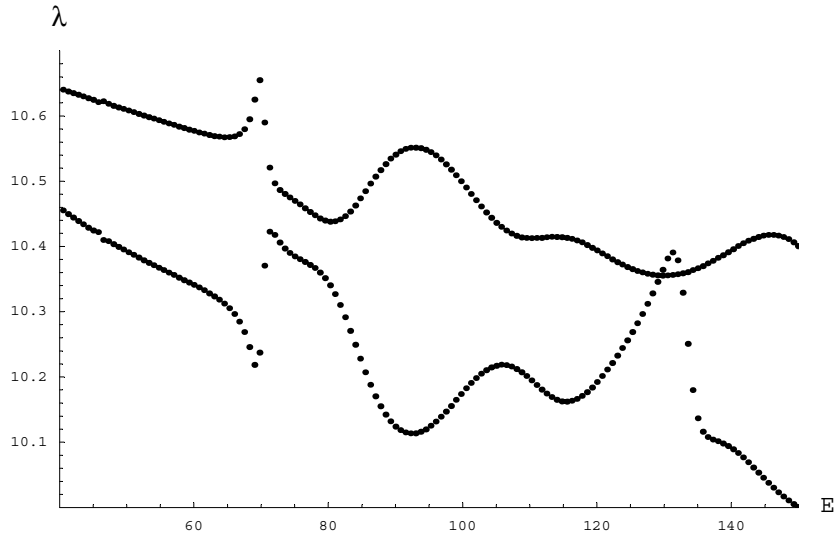

Figure 3. Total differential cross section on-axis (upper) and 30° off-axis (lower) for the three-peaked scatterer, given in figure 1, with $V_o = 1200$, $a = 1.6$ and $R = 2.5$.

complex plane,

$$E \to E_r - i\Gamma/2; \qquad 0 < E_r, \quad 0 < \Gamma. \tag{22}$$

Because on-shell terms are no longer needed and the Green's function is nonsingular for complex energies, the radial integration may be truncated where contributions from the integrand are no longer significant. Near E, however, the integrand will vary rapidly as the complex energy approaches the real axis. To treat this region, we exploit the fact that the numerator of the integrand is still smooth and apply a Taylor–Laurent series expansion,

$$\int_{E_1}^{E_2} \frac{f(E')}{E-E'}\,dE' = \int_{E_1}^{E-\varepsilon_1} \frac{f(E')}{E-E'}\,dE' + \int_{E+\varepsilon_2}^{E_2} \frac{f(E')}{E-E'}\,dE' + \int_{E-\varepsilon_1}^{E+\varepsilon_2} \frac{1}{E-E'} \times \left[f(E) + (E'-E)f'(E) + \frac{(E'-E)^2}{2} f''(E) + O(E'-E)^3 \right] dE' \tag{23}$$

(here $\mu\,dE' = \hbar^2 k'\,dk'$), for which now

$$E = \left(k_{or}^2 - k_{oi}^2, 2k_{or}k_{oi}\right) \in \mathcal{Z}, \tag{24}$$

giving this expansion both a real and an imaginary part. Uniform radial intervals in k-space of width $\sqrt{\varepsilon_2} - \sqrt{\varepsilon_1}$ were used which allow for the determination of $f(E)$ in (23), along with its first and second derivatives, through the simultaneous solution of the following three approximations:

$$\begin{aligned} f(E_{p-1}) &\approx f(E) + (E_{p-1}-E)f'(E) + \frac{(E_{p-1}-E)^2}{2} f''(E), \\ f(E_p) &\approx f(E) + (E_p-E)f'(E) + \frac{(E_p-E)^2}{2} f''(E), \\ f(E_{p+1}) &\approx f(E) + (E_{p+1}-E)f'(E) + \frac{(E_{p+1}-E)^2}{2} f''(E). \end{aligned} \tag{25}$$

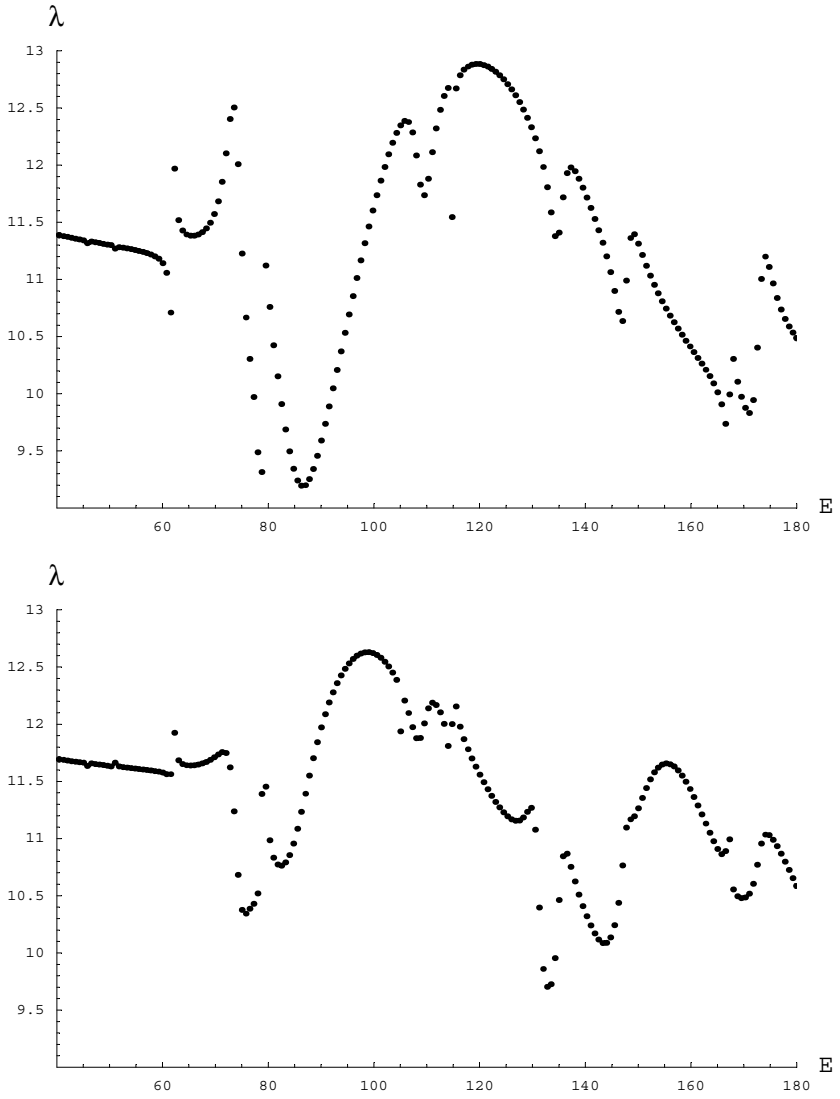

Figure 4. Total differential cross section on-axis (top) and 15° off-axis (bottom) for the four-peaked scatterer (26) with $V_o = 1200$, $a = 1.6$ and $R = 2.5$.

The resulting three complex integrals represented by the last term of (23) are easily evaluated and we then proceed to assemble the inverse wave operator Ω_E^{-1}. It would be possible to use an expansion of higher order, but nothing would be gained since a trapezoidal rule is used for the remainder of the radial integration for which the error is proportional to $(\Delta k)^2$.

The discretized characteristic equation (10) must have N roots. Most of these solutions will not be resonances but rather artefacts of the discretization. These artificial roots are expected to lie near the real axis between the discrete grid points. They are related to the approximate representation of the potential as the sum of delta functions along the real axis. Actual resonances may be recognized from their independence of the numerical implementation and from widths that decrease with increasing potential heights.

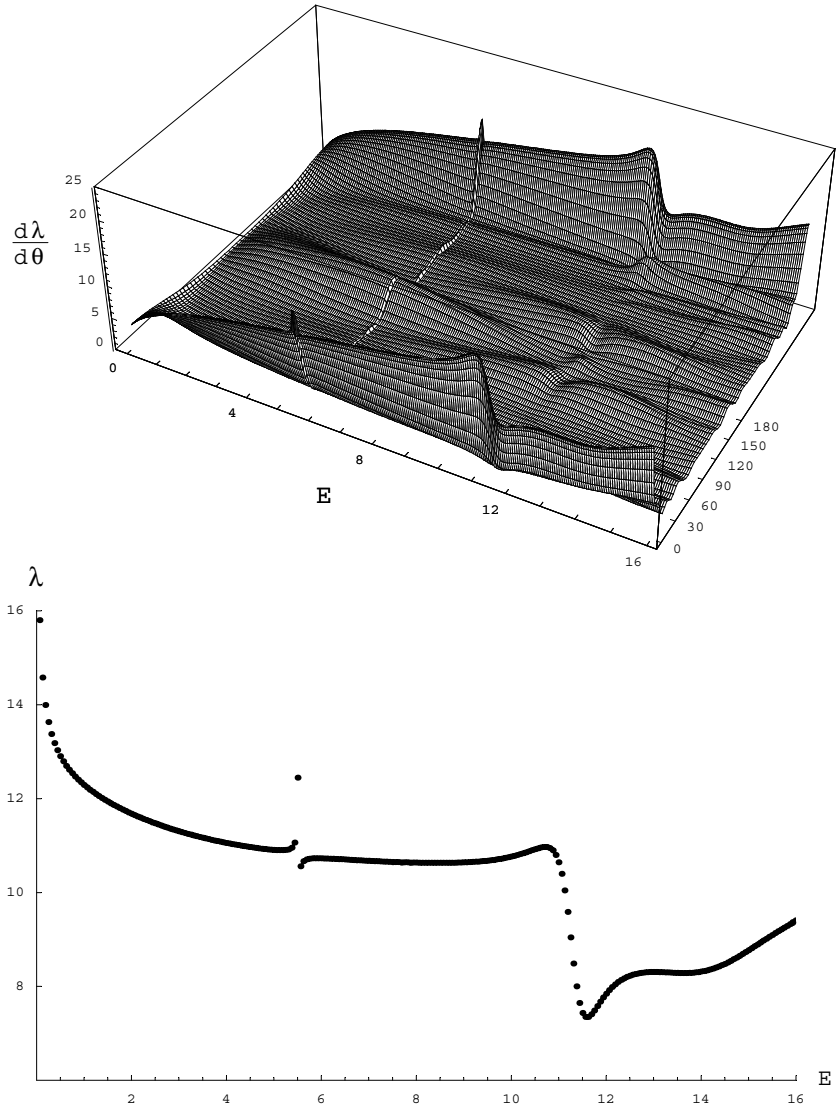

Figure 5. Differential cross-sectional surface (top) with the corresponding integrated total cross section (bottom) for (26) with $V_o = 100$, $a = 1.6$, $R = 2.5$ and an incident angle of 0° with the x-axis.

To confirm our resonances, we required verification from a second code that was written using the alternate identity (19) for regularization. For this code, the on-shell momenta were retained and an irregular radial grid spacing of Gauß–Legendre points on $[0, \infty)$, as required by the subtraction method, replaced the truncated radial points of uniform spacing from the code discussed above. Both codes were specifically designed to find the zeros of a system of n nonlinear functions in n variables through the use of a modified Powell hybrid method. In our case $n = 2$, where the real and imaginary parts of the determinant (10) are functions of the real and imaginary parts of the analytically continued energy, E.

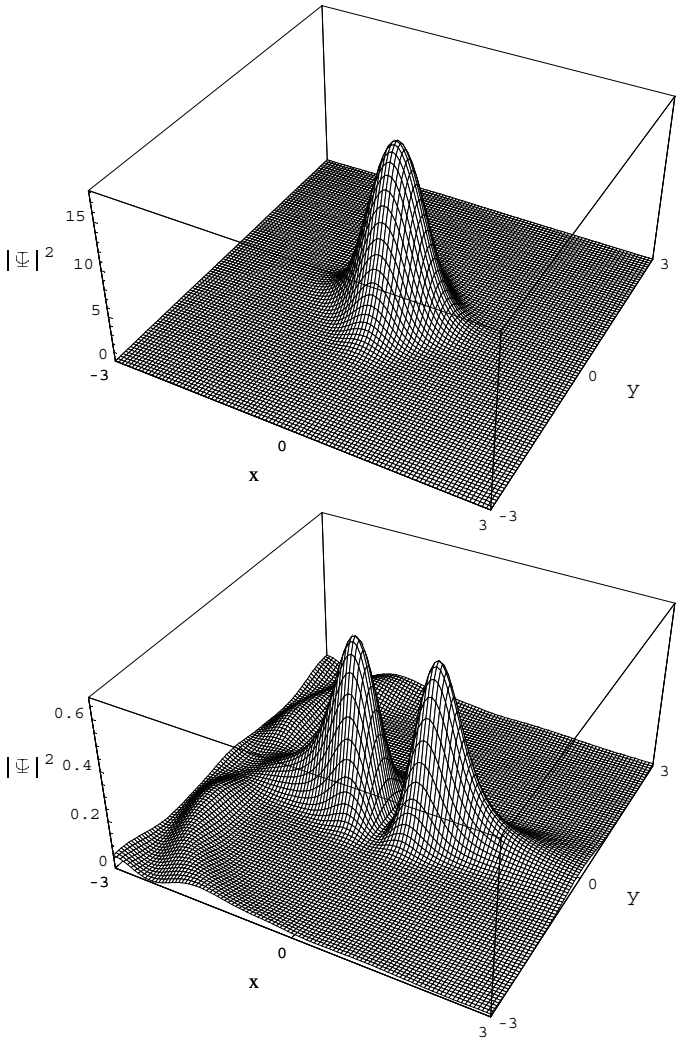

Figure 6. Probability density for the first (A_1 symmetry) and second (E symmetry) resonances in table 4 for which $V_o = 100$, $a = 1.6$ and $E = 5.513\,05$ (top), $E = 11.3781$ (bottom).

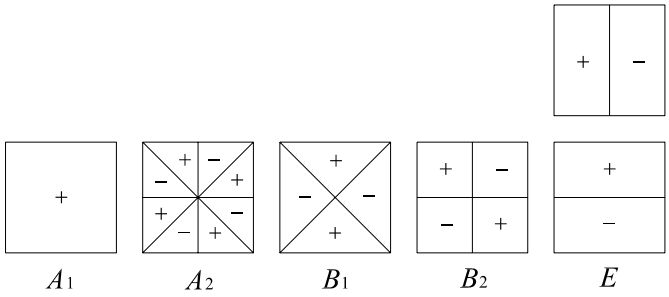

Figure 7. D_4 irreducible abstract representations.

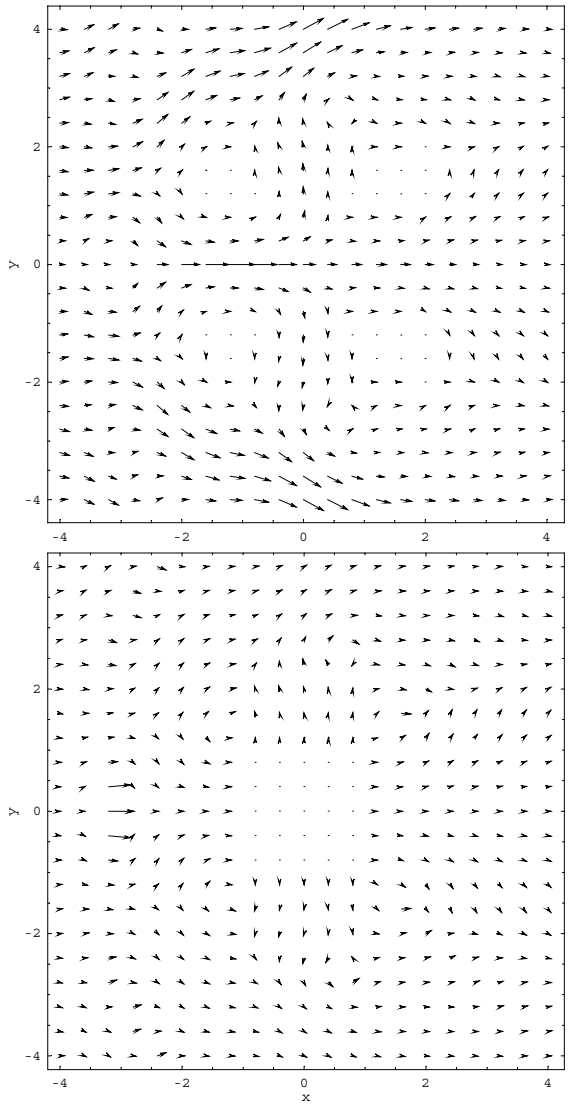

Figure 8. Vector fields representing current density (top) and velocity (bottom) of the fundamental resonance (table 4) calculated from (7). Vector lengths are relative, the longest being scaled to the radius of a circle determined by the bases of the nearest neighbours. Vectors are suppressed for any magnitudes below a cut-off threshold of 0.061% (current) and 0.300% (velocity) of maximum.

We did not seek to find all the resonances in the complex plane. Because we lacked any prior knowledge of resonance positions for the unfamiliar systems investigated, we would ideally initialize independent searches on the vertices of a hypothetical grid placed over the complex energy plane. If the grid were tight enough, we would expect that the result would be overlapping neighbourhoods of searched areas for which we would have exhausted the possible dwellings of any elusive poles. In reality, however, we lacked the resources for such an extensive search, so we had to settle for an alternate plan. This was to look for signatures of long-lived resonances in the cross sections and initialize searches only in their immediate neighbourhoods.

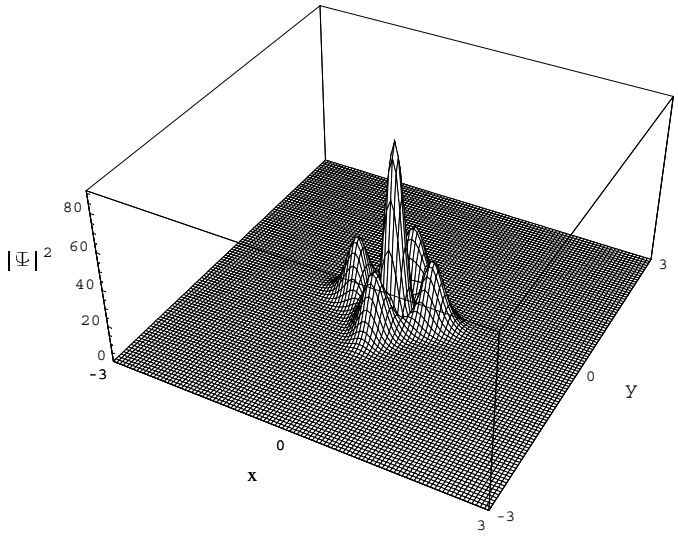

Figure 9. Probability density for the fourth resonance of table 4 for which $V_o = 1200$, $a = 1.6$ and $E = 50.9141$ with normal incidence.

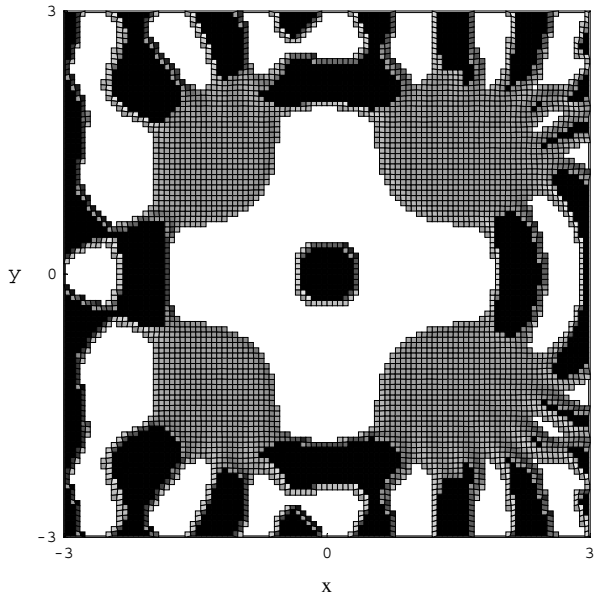

Figure 10. Real part of the fourth resonance's clipped wavefunction showing the second A_1 symmetry (note the single nodal ring at fixed radius). Black $< -0.002 \leqslant$ grey $\leqslant 0.002 <$ white (top). The incident plane wave is seen to approach from the left.

3.2. Scattering potentials

The potentials chosen were repulsive three- and four-centre scatterers defined by overlapping Gaussian peaks, each of height V_o and width $1/a$, lying on the vertices of an equilateral triangle

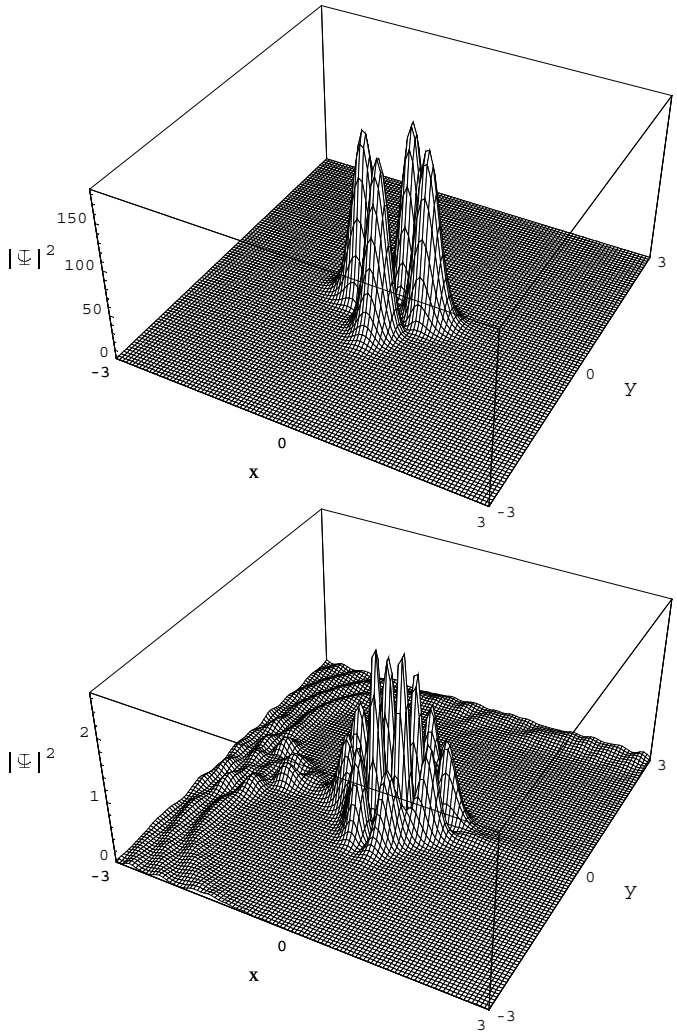

Figure 11. Probability density for the third (B_1 symmetry) and eighth (B_2 symmetry) resonances in the D_4 table for which $V_o = 1200$, $a = 1.6$ and $E = 45.7994$ (top), $E = 105.017$ (bottom).

or a square with sides of length R. The square, for example, will have the form

$$V(\mathbf{r}) = \frac{V_o}{\exp\left(\left[a\left(x-\frac{R}{2}\right)\right]^2+\left[a\left(y+\frac{R}{2}\right)\right]^2\right)} + \frac{V_o}{\exp\left(\left[a\left(x+\frac{R}{2}\right)\right]^2+\left[a\left(y-\frac{R}{2}\right)\right]^2\right)} + \frac{V_o}{\exp\left(\left[a\left(x+\frac{R}{2}\right)\right]^2+\left[a\left(y+\frac{R}{2}\right)\right]^2\right)} + \frac{V_o}{\exp\left(\left[a\left(x-\frac{R}{2}\right)\right]^2+\left[a\left(y-\frac{R}{2}\right)\right]^2\right)}, \tag{26}$$

with a momentum-space representation, required for equations (11), (13) and (20), given by

$$V(\mathbf{k},\mathbf{k}_o) = \frac{V_o}{\pi a^2}\left(\frac{\cos\left[\frac{R}{2}(k_x-k'_x)\right]\cos\left[\frac{R}{2}(k_y-k'_y)\right]}{\exp\left[\frac{(k_x-k'_x)^2+(k_y-k'_y)^2}{4a^2}\right]}\right). \tag{27}$$

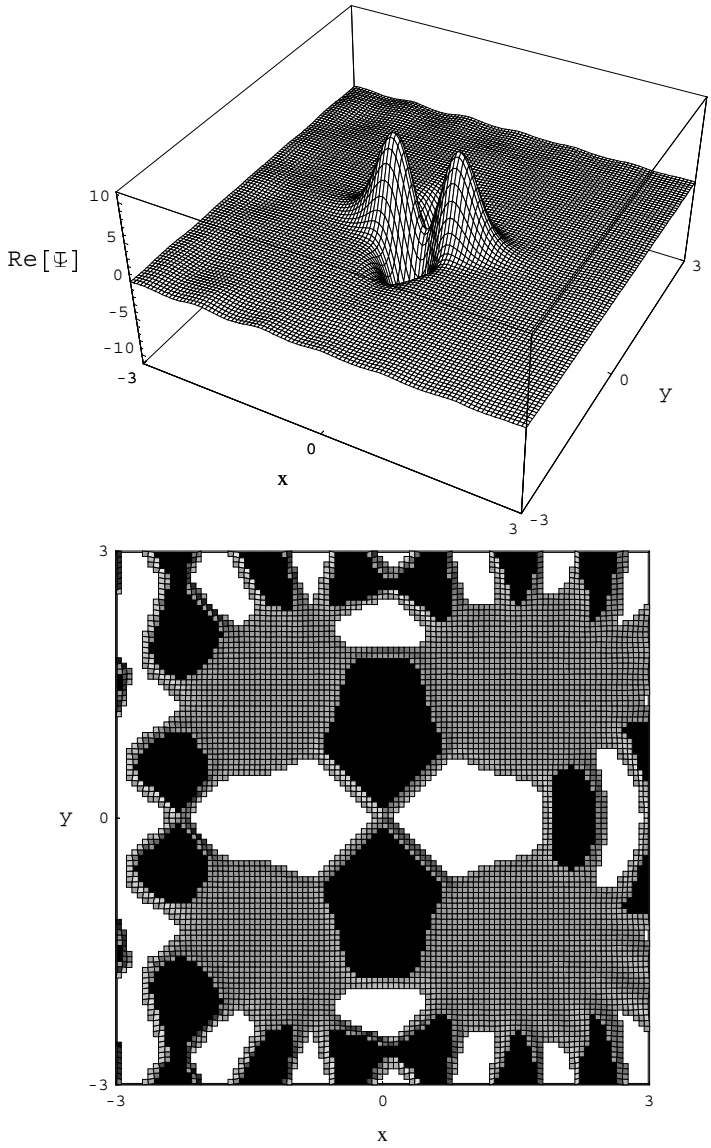

Figure 12. Real part of the third resonance's wavefunction for which $V_o = 1200, a = 1.6$ and $E = 45.7994$. Bottom clipped so that black $< -0.01 \leqslant$ grey $\leqslant 0.01 <$ white.

The momentum-space representation for the triangular potential will have an additional imaginary term due to its lower symmetry. The potentials are plotted in figures 1 and 2 with the parameter values, $R = 2.5$ and $a = 1.6$, chosen for this paper. The potential heights have been scaled down from the two values, $V_o = 100$ and $V_o = 1200$, considered. We were able to further validate results by reproducing published resonances for three and four hard discs [10, 11]. The technique of mimicking hard discs with Gaussians involves the continual fitting of phase shifts between a hard disc and a single Gaussian in the limit of increasing height through the adjustment of the free parameters.

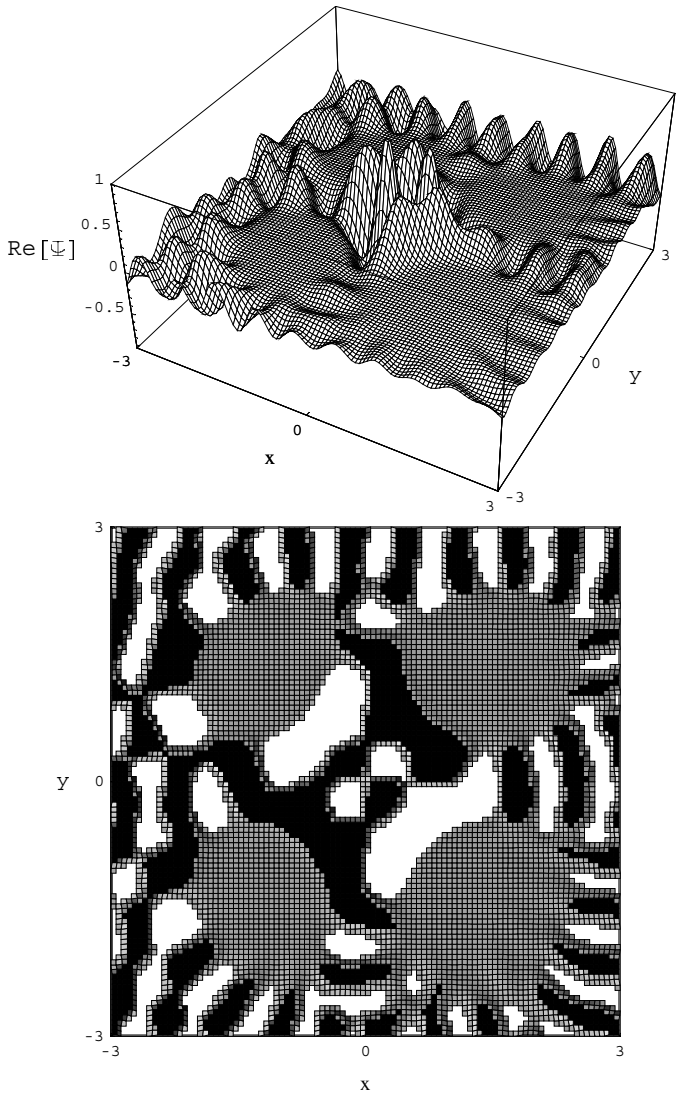

Figure 13. Real part of the eighth resonance's wavefunction for which $V_o = 1200$, $a = 1.6$ and $E = 105.017$. Bottom clipped so that black $< -0.01 \leqslant$ grey $\leqslant 0.01 <$ white. Here the incident angle is $\theta_o = \pi/12$.

4. Results and discussion

The spatial dependence of these noncentral potentials allows low-energy quantum particles to be briefly trapped between the peaks within their central region. The degree of trapping of these resonant states may be determined from their widths and the probability densities. For a narrow resonance the trapping is more stable, and the magnitude of the wavefunction at the centre of the potential is large relative to the incident plane wave, resembling a bound state. For this reason, we expect the wavefunction within the scatterer's interior to exhibit symmetry properties reflecting those of the potential, described by the dihedral groups D_3 and D_4, characteristic of an equilateral triangle and a square. The character tables 1 and 2, for

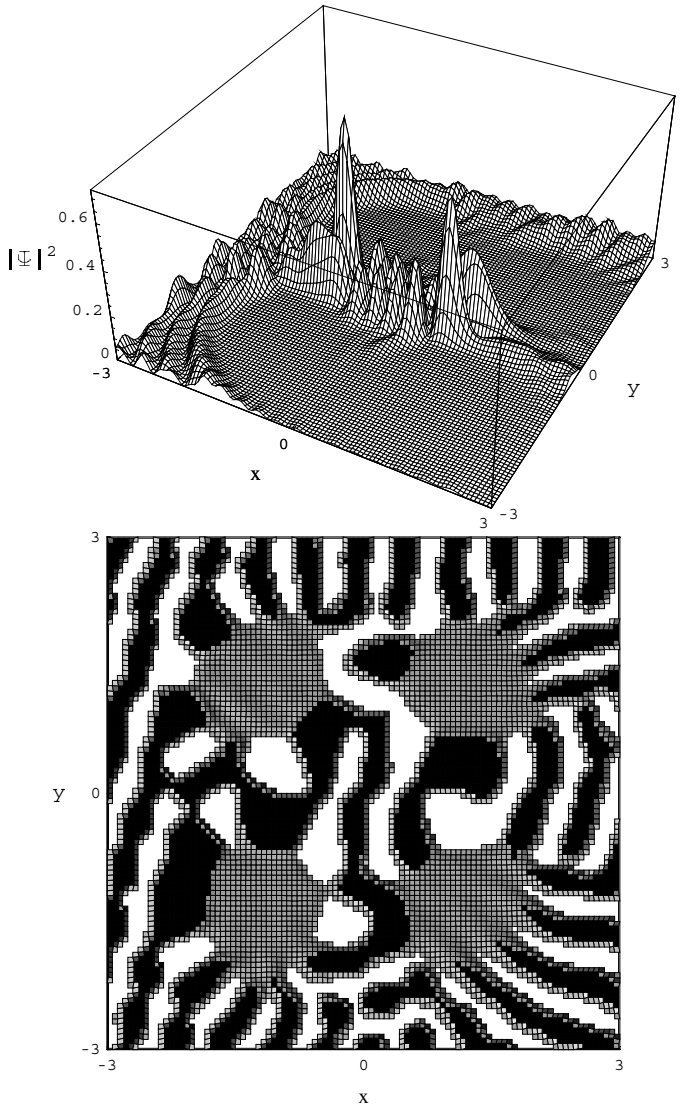

Figure 14. Probability density (top) and real part of the clipped (black $< -0.002 \leqslant$ grey $\leqslant 0.002 <$ white) wavefunction (bottom) for the 11th resonance of table 4 showing A_2. Here $V_o = 1200$, $a = 1.6$, $E = 131.429$ and the incident angle is $\theta_o = \pi/12$.

Table 1. D_3 dihedral character table.

C_{3v}	E	$2C_3$	$3\sigma_v$
A_1	1	1	1
A_2	1	1	-1
E	2	-1	0

these specific groups are given with the irreducible symmetry representations labelled by the appropriate Mulliken symbols.

Table 2. D_4 dihedral character table.

C_{4v}	E	$2C_4$	C_2	$2\sigma_v$	$2\sigma_d$
A_1	1	1	1	1	1
A_2	1	1	1	−1	−1
B_1	1	−1	1	1	−1
B_2	1	−1	1	−1	1
E	2	0	−2	0	0

Table 3. First three 'long-lived' resonances for the three-peaked scatterer with $a = 1.6$ and $R = 2.5$.

V_o	E	$\Gamma/2$	k_r	k_i	Order	Symmetry
1200	46.1718	4.0252×10^{-3}	6.7950	2.9617×10^{-4}	1	A_1
1200	69.9163	1.0250×10^{0}	8.3618	6.1292×10^{-2}	2	E
1200	133.264	3.8954×10^{0}	11.545	1.6870×10^{-1}	1	A_2

Table 4. First 13 'long-lived' resonances for the four-peaked scatterer (26) with $a = 1.6$ and $R = 2.5$.

V_o	E	$\Gamma/2$	k_r	k_i	Order	Symmetry
100	5.513 05	8.0678×10^{-3}	2.3480	1.7180×10^{-3}	1	A_1
100	11.3781	2.5449×10^{-1}	3.3734	3.7775×10^{-2}	2	E
1200	45.7994	1.5048×10^{-3}	6.7675	1.1118×10^{-4}	1	B_1
1200	50.9141	5.6243×10^{-3}	7.1354	3.9411×10^{-4}	1	A_1
1200	61.8927	1.2089×10^{-1}	7.8672	7.6834×10^{-3}	2	E
1200	74.0325	4.1675×10^{0}	8.6076	2.4208×10^{-1}	1	A_1
1200	78.8937	5.4588×10^{-1}	8.8823	3.0728×10^{-2}	2	E
1200	105.017	8.3296×10^{-3}	10.248	4.0641×10^{-4}	1	B_2
1200	109.108	1.2639×10^{0}	10.447	6.0501×10^{-2}	1	?
1200	114.780	1.7712×10^{-1}	10.715	8.2660×10^{-3}	2	E
1200	131.429	1.1741×10^{0}	11.464	5.1208×10^{-2}	1	A_2
1200	134.587	1.1474×10^{0}	11.601	4.9450×10^{-2}	2	E
1200	147.285	1.0664×10^{0}	12.136	4.3936×10^{-2}	1	B_1

For each potential, we calculated differential and total cross sections for both normal and off-axis incidence with respect to a lateral face of the geometric figure defined by the particular potential. As in the rest of this paper, results are displayed for the elastic channel only with the following choice for energy units:

$$2\mu = \hbar^2 \quad \Rightarrow \quad E = k_o^2. \tag{28}$$

The resulting length scale, $\lambda = 2\pi/\sqrt{E}$, is included with all spatial plots for comparison with figures 1 and 2. The total cross sections are given in figures 3 and 4 from which the prominent peaks have been used to tabulate the resonances appearing in tables 3 and 4. For the square potential, peaks in the cross sections belonging to the two lowest resonances are too narrow to discern. Because their energies fall below the saddle points occurring between Gaussians, they correspond to classically bound states. The first is comprised of a half wavelength internal to the potential's four peaks. The next higher energy configuration carries a full wavelength in the incident direction while retaining a half wavelength in the orthogonal direction. Additional cross sections are provided in figure 5 for a reduced potential height of $V_o = 100$ for which

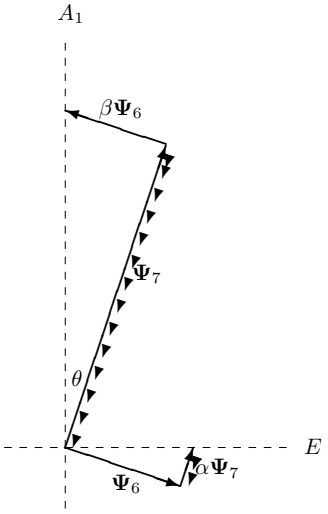

Figure 15. Schematic for the rotation of the real parts of mixed state vectors, neglecting normalization, belonging to the sixth and seventh resonances.

the saddle points, at an energy of $E = 3.7$, now fall below the two lowest resonances whose peaks are now clearly visible. Note that the differential cross section becomes angle independent for very low energy scattering, as expected. The probability densities of these first two resonances are given in figure 6. From the visual renderings of square symmetries given in figure 7, it is evident that the first wavefunction possesses A_1 symmetry while the second belongs to the two-dimensional representation E. Vector plots of the current density and velocity field calculated from (7) for the fundamental resonance have been included, figure 8, to show that the more stable resonances correspond to classical multiple-reflection events. Flow is maintained across the scatterer at these resonances but the velocity drops off due to the large probability density peaks within the scatterer's interior region, indicative of particles undergoing numerous reflections within the potential before escaping.

The orders given in tables 3 and 4 show that wavefunction symmetries belonging to the two-dimensional E representation are degenerate and correspond to double poles of the wave operator. The order of each pole is determined by evaluating the determinant $\left|\Omega_E^{-1}\right|$ on a ring, with a small radius, of complex energies that encompass the energy of the pole. In a small neighbourhood about the pole, the complex function will be governed by the pole structure and the function $g(z)$ may be taken to vary slowly enough that it can be approximated by a constant on a ring with a sufficiently small radius.

$$f(z) = \frac{g(z)}{(z - z_o)^n} \quad \underset{z \to z_o}{\longrightarrow} \quad \frac{C\, e^{in\theta}}{\|z - z_o\|^n}. \tag{29}$$

When graphing the real and imaginary parts of the determinant on the periodic interval $[0, 2\pi]$, each part will exhibit an even number of sign changes, returning to the initial value. The order of the pole is equated with the number of pairs of sign changes.

The fourth tabulated resonance of the quad-peaked scatterer represents the second occurrence of A_1 symmetry. It is narrower, with a larger probability density (figure 9), than the first only because the potential height has been increased by a factor of 12. It also possesses a radial nodal ring which is clearly visible from the wavefunction (figure 10). Each successive A_1 resonance of higher order will carry with it an additional nodal ring.

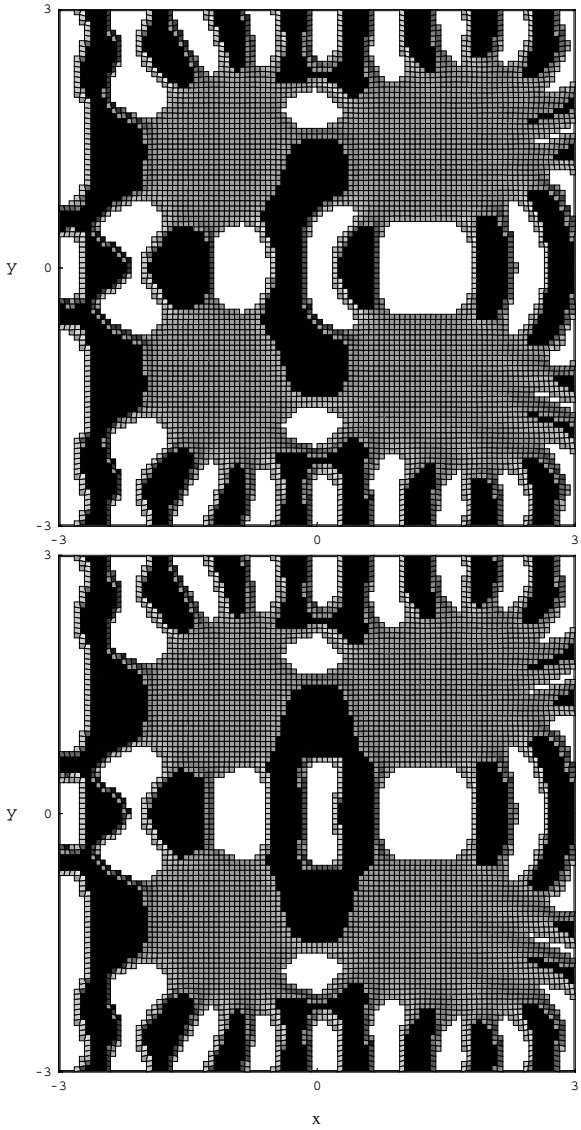

Figure 16. Real (top) and rotated (bottom) part of the sixth resonance's clipped wavefunction showing A_1 symmetry. Black $< -0.005 \leqslant$ grey $\leqslant 0.005 <$ white (top). The incident plane wave is seen to approach from the left.

Probability densities for the third and eighth tabulated resonances of the square scatterer which carry B-type symmetry, specifying a singly degenerate state which is antisymmetric with respect to rotation of $\pm\pi/2$ about the principal axis normal to the scattering plane, are shown in figure 11. Unlike for hard cage potentials, the longest lived resonances of soft cages will in general grow wider with energy as the intercolumniation increases. The wavefunction of the more stable B_1 resonance, for which the real part is given in figure 12, is generated with normal incidence. As is evident from the character tables and symmetry renderings, tables 1 and 2 and figure 7, the mirror symmetry about the centreline must be broken to excite

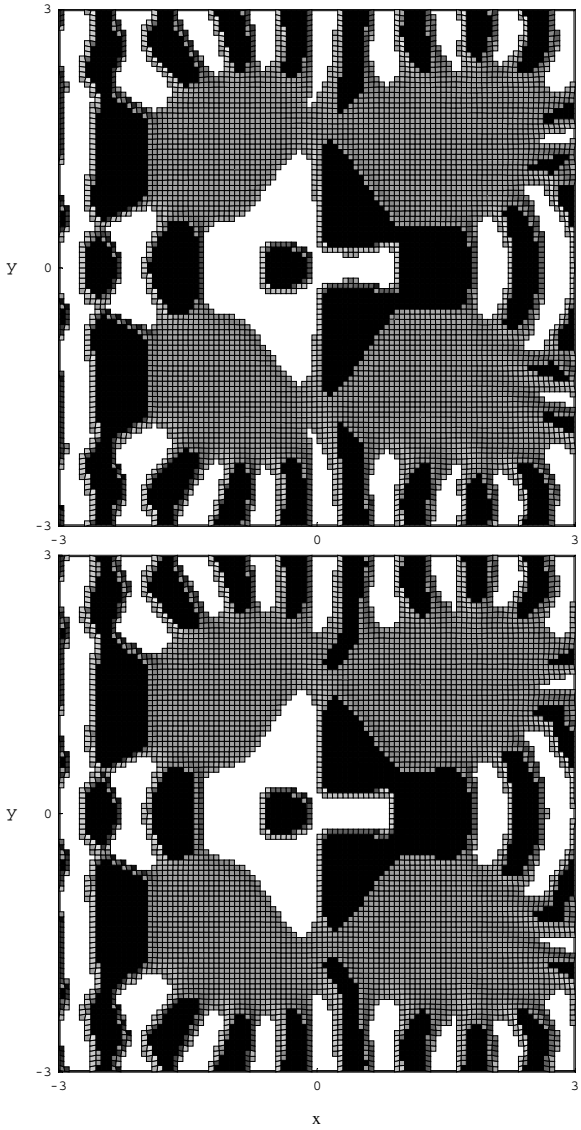

Figure 17. Real (top) and rotated (bottom) part of the seventh resonance's clipped wavefunction showing E symmetry. Black $< -0.005 \leqslant$ grey $\leqslant 0.005 <$ white (top). The incident plane wave is seen to approach from the left.

the A_2 and B_2 resonances. This can also be seen from the cross sections given in figures 3 and 4. For this reason, probability densities and wavefunctions generated for the 8th and 11th resonances, given in figures 13 and 14, were done so with an angle of incidence 15° off the axis normal to the potential's left square face. Because the 11th resonance of table 4 has a relatively short lifetime as compared to some of the others, the symmetry-breaking effects of the incident wave are no longer negligible.

The irreducible representations comprise a type of symmetry basis from which less symmetric waves may be constructed, such as those belonging to the sixth and seventh

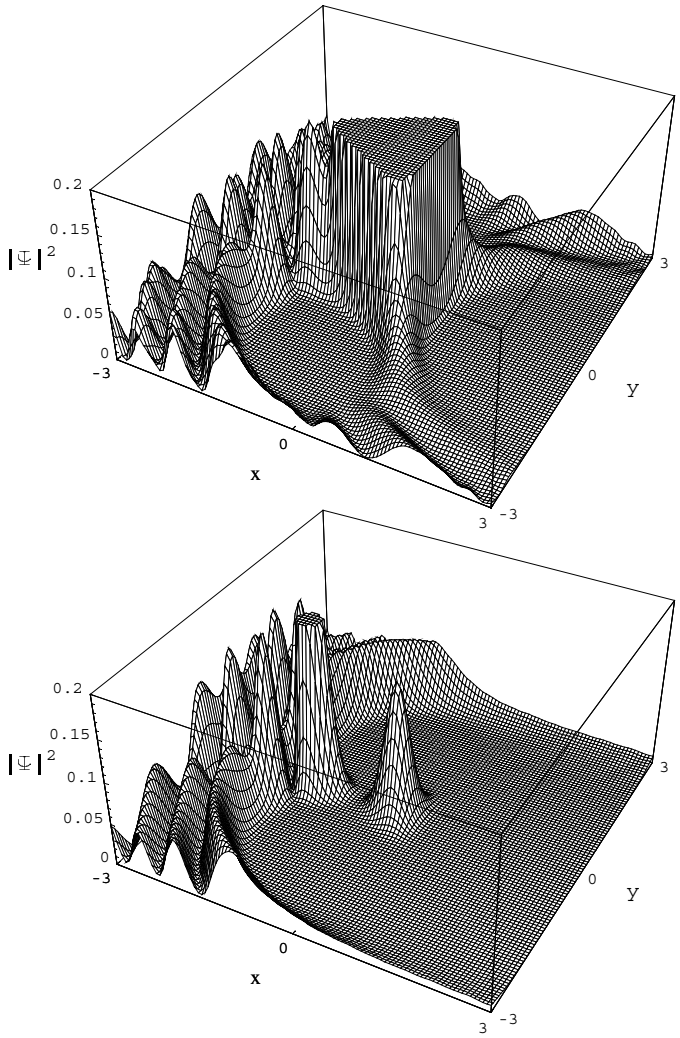

Figure 18. Clipped probability density for the first resonance of table 3 for which $V_o = 1200$, $a = 1.6$ and $E = 46.1718$ with normal incidence (top). Note that at the slightly higher energy of $E = 46.3500$ (bottom), the particle flux is much less effective at penetrating the interior region of the potential despite the shorter wavelength.

resonances from table 4. We note from table that the spacing between these two resonances is similar to the width of the lower one. A hybridization of wavefunction symmetries is thus expected for the overlapping resonances. This mechanism is somewhat analogous to one that was offered by Ericson and others [16–18], during the early part of the 1960s, as an explanation for fluctuations appearing in nuclear cross sections for transition state spectroscopy experiments. The assumption is that a group of resonances may exist whose widths exceed nearest-neighbour spacings. From the energy uncertainty argument, $\Delta E \Delta t \geqslant \hbar/2$, all the intermediate states within the group are interpreted as being simultaneously populated. The consequent interference results in the Ericson fluctuations appearing in cross sections (compare this with figure 4).

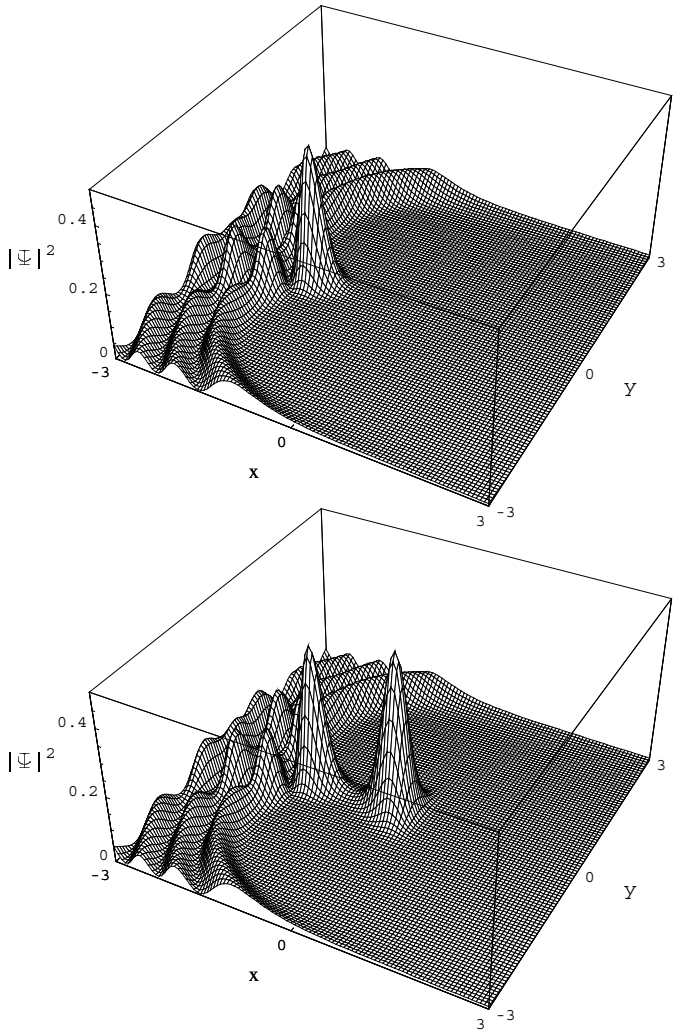

Figure 19. Probability density below, $E = 45.0$ (top) and $E = 46.0725$ (bottom), the fundamental resonance, $E = 46.1718$ (table 3), for $V_o = 1200$ with a normal angle of incidence. Note that the particle flux is at first unable to penetrate into the potential's interior region.

Upon investigating the wavefunctions of the sixth and seventh tabulated resonances, we find their real parts to be more strongly mixed than the imaginary parts for which hybridization is minimal. We attempt to separate the real parts of the wavefunction and reveal their symmetry by a rotation of the state vectors. As diagrammed in figure 15, we add to each real part a piece of the other,

$$\mathrm{Re}(\Psi_{6'}) = \mathrm{Re}(\Psi_6) + 0.08\,\mathrm{Re}(\Psi_7), \qquad \mathrm{Re}(\Psi_{7'}) = \mathrm{Re}(\Psi_7) - 0.2\,\mathrm{Re}(\Psi_6). \tag{30}$$

Because the seventh tabulated resonance is comparatively much narrower than the sixth, Ψ_7 will be larger than Ψ_6 in the region internal to the scatterer. The resulting representative vectors, shown in figure 15, thus have different lengths and we expect their ratio to be similar to that of the coefficients α and β given in (30). We point out that because the scattering

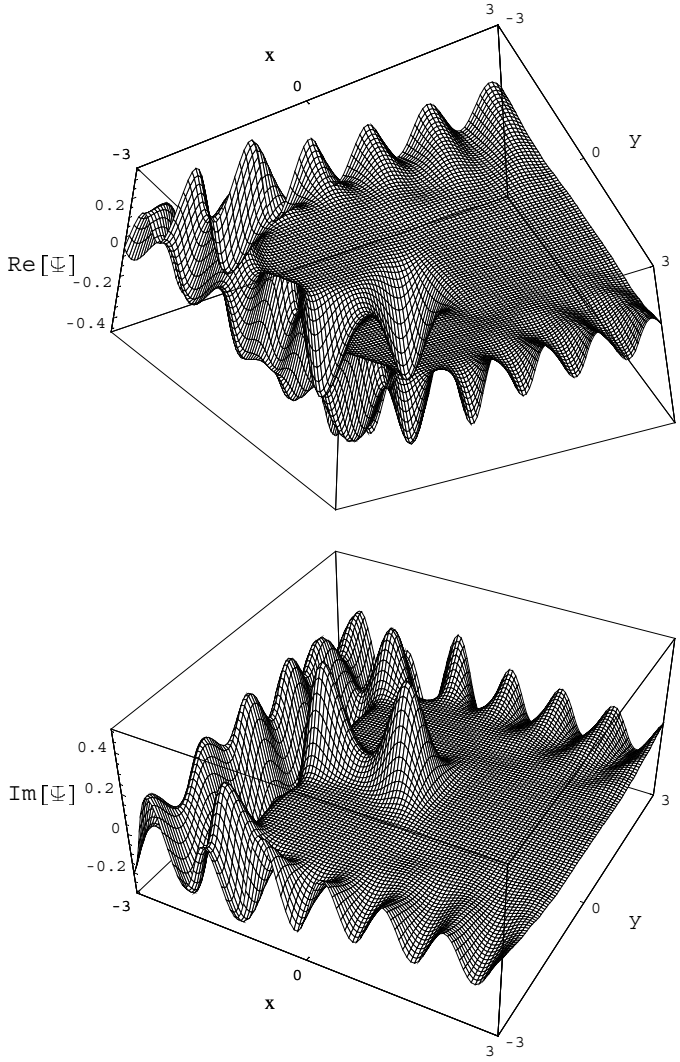

Figure 20. Real (viewed from underneath) and imaginary (bottom) parts of the wavefunction below, $E = 46.0725$, the fundamental resonance of $E = 46.1718$ (table 3) for $V_o = 1200$ with a normal angle of incidence showing quantum pinching.

wavefunctions are not square-integrable, they are not normalizable in the conventional sense. In figure 16, we display the real part of the wavefunction for the sixth resonance both before and after rotation. In figure 17, we do the same for the seventh. After rotation, we see that the real part of the sixth resonance displays the angular independence of the A_1 representation. Being the third occurrence of this representation, we expect to see two nodal rings. The symmetry is not as evident as others displayed due to distortions stemming from the fact that this is among the two widest resonances, resulting in a larger symmetry-breaking effect of the incident wave. In figure 17, we see that the vertical line of reflection, as well as the horizontal nodal lines, has become slightly cleaner after rotation. Being the narrower of the two resonances, the changes are relatively small.

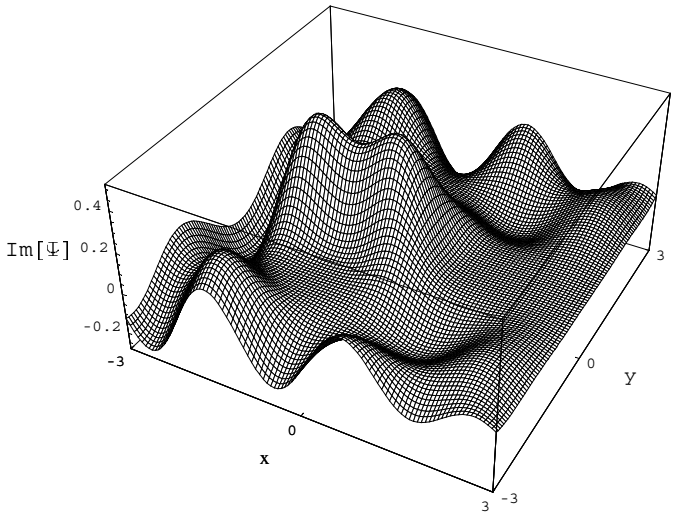

Figure 21. Imaginary part of wavefunction for the three-centre scatterer below, $E = 9.56$, the fundamental resonance of $E = 9.8326$ for $V_o = 100$ with a normal angle of incidence showing quantum pinching.

In the upper plot of figure 18, we show the probability density peak of the fundamental resonance from table 3 scaled to clearly show the leaking of probability from inside the cage out around the potential's exit pillar. The lower plot shows the probability, scaled to the same ratio with respect to the incident wave, for a slightly higher energy for comparison. With a shortening of the wavelength, one might naively expect that transmission of the incident wave through the potential would be improved at an increased energy since the wavefunction would seem to fit between the pillars more easily. As the lower plot shows, however, this is not the case. As the energy moves off resonance, the transmission of the incident wave through the potential drops off drastically. This is in agreement with results reported by Peskin *et al* [6] for resonant transmission through water.

At an energy of $E = 45.0$ for the three-centre potential, slightly lower than the fundamental resonance, we see from the probability density, upper plot of figure 19, that the transverse wavelength is such that ingress between the potential's entrance pillars is not possible and a strong reflection peak builds in front of it. As the energy increases toward resonance, we see from the lower plot that particles, with wavelengths that are still seemingly too large, are able to squeeze through the narrow passage into the scatterer's interior region. This occurs at the expense of the longitudinal wavelength. Energy being conserved, the longitudinal wave number, $k_l = \sqrt{E - k_t^2}$, goes imaginary as the transverse wavelength shortens, allowing for passage. This *quantum pinching* effect is evident from the longitudinal curvature away from the $z = 0$ plane and simultaneous transverse narrowing which can be seen from the wavefunction between the entrance pillars given by figure 20. Figure 21 shows quantum pinching again for a lower potential height, $E = 100$, and the same value for the width parameter, $a = 1.6$. This quantum pinching has also been demonstrated for the first two resonances in table 4, establishing it as a universal feature.

From more panoramic views of the probability densities, such as the one given in figure 22, one can see clear dips in the particle densities behind the scatterer. These shadows, opposite to the incident wave, have also been seen and reported for azimuthally symmetric

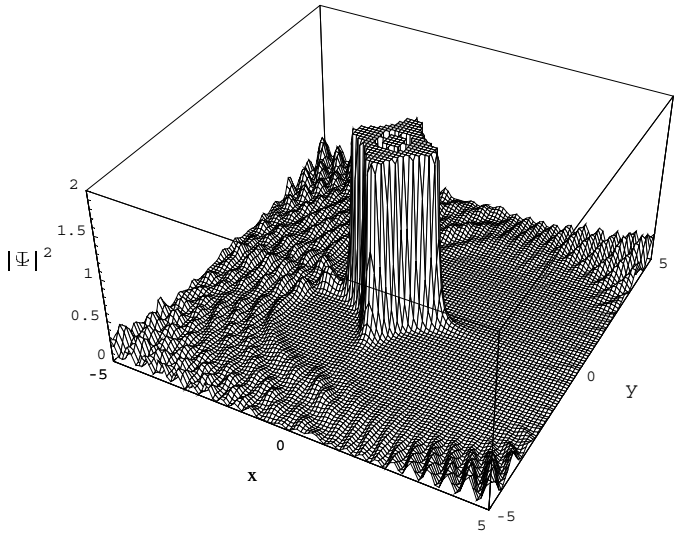

Figure 22. Panoramic probability density for the fourth resonance of table 4 for which $V_o = 1200, a = 1.6$ and $E = 50.9141$ showing a complicated interference pattern and the shadow behind the scatterer opposite to the incident wave. Truncation of the probability peak here shows the dip in particle densities forming a circular pattern.

scatterers [19]. In addition to the shadowing phenomenon, these panoramic views display the complex interference patterns that result between the incident and scattered waves.

Since energies considered have been low as compared to the heights of the potentials, we expect the wavefunctions to essentially vanish near the centres of the Gaussian regions. The computed wavefunctions are small in these regions because of interference between the incident and scattered waves and are not due to an imposed boundary condition. The resulting areas which are flat with respect to the incident waves in the wavefunction figures provided us with the means to estimate the accuracy of our computations which we placed at within 0.003% and 0.12% for the lowest and highest energies, respectively. This is accomplished by tracking the break-up of the grey areas in clipped wavefunction plots, like those shown in figures 12–14, as the 'slices' become thinner.

5. Conclusions

Present-day manufacturing abilities now include micro-optic and nano-electronic devices. On these length scales, low-mode quantum effects cannot be excluded. A clear understanding is required for wave trapping within potentials that reflect the structure of such devices. The objective of this work has been to contribute to the understanding of the nature of low-energy scattering wavefunctions that result from soft repulsive potentials with broken angular symmetries.

We have demonstrated that the geometry of two-dimensional cage potentials allows long-lived resonances. Such states arise from the transient trapping of quantum particles between the peaks of the potential and correspond classically to multiple reflection. This verifies, for our simple geometry, the interpretations by Peskin *et al* [6] that transmission maxima correspond to scattering resonances and that the corresponding localized enhancement in the probability density is due to the local geometry of the scattering centres.

Because of their spatial dependence, soft cage potentials have openings between peaks (the distances between level curves above the saddle points) that broaden with increasing energy. As a result, resonance widths have a strong energy dependence not seen for similar hard potentials that have energy-independent intercolumniation. For hard potentials of this type, there are no resonances in a gap of approximately uniform width below the positive real momentum axis. The width of this band depends not on the energy [10, 11], but on the distance between scattering centres, or more specifically the separation between columns which determines the degree of trapping. For soft potentials, however, we have shown that the width of this gap increases with energy leading to shorter lifetimes for higher energy resonances.

That specific low-energy resonances with very narrow width correspond to classical multiple-reflection events is evidenced by much larger probability densities inside the cage than outside, with averaged velocity fields that drop significantly inside the cage as current density actually increases there. These states mimic bound states in the sense that the symmetry-breaking effect of the incident wave is minimal. As a result, we have found that these states display the simple symmetry characteristics of bound states.

An example has also been presented in which one of the pair of neighbouring resonances has a width that is nearly equal to the interresonance spacing. Under these circumstances, the resulting hybridization is shown to cause a mixing of symmetry classes leading to wavefunctions of lower symmetry, like those exhibited for wider resonances at higher energy.

We have demonstrated that at energies below the lowest resonances of two-dimensional cages, where the distance across the entrance of the cage corresponds to less than half a wavelength, the wavefunction may still gain access to the interior region by squeezing its wavelength in the necessary direction at the expense of the kinetic energy in the direction normal to the opening. The resulting curvature in the donor dimension corresponds to an imaginary wave number, curving away from the xy-plane. It would be interesting to replace the potentials used for this work with a lattice of repulsive scattering centres to investigate wavefunction transmission at and off resonance for a geometry that more closely resembles the structure of electronic nanocircuits or photonic crystal fibres.

Acknowledgments

The research reported in this paper was conducted for a PhD thesis at Oregon State University. Readers interested in a more complete account of this research, including higher resolution plots, are encouraged to request a copy of the dissertation by e-mailing kirkrowe@lifetime.oregonstate.edu.

References

[1] Elenbogen J C 1998 *A Brief Overview of Nanoelectronic Devices: 1998 Government Microelectronics Applications Conference (GOMAC98)* © 1998 by the Mitre Corporation

[2] Russell P 2003 Photonic crystal fibers *Science* **299** 358–62

[3] Botten L C, McPhedran R C, Nicorovici N A, Asatryan A A, de Sterke C M, Robinson P A, Bush K, Smith G H and Langtry T N 2003 Rayleigh multipole methods for photonic crystal calculations *Prog. Electromagn. Res.* **41** 21–60

[4] Arriaga J, Knight J C and Russell P J St 2003 Modeling the propagation of light in photonic crystal fibers *Physica* D **189** 100–6

[5] Blaze Photonics www.blazephotonics.com

[6] Peskin U, Edlund A, Bar-On I, Galperin M and Nitzan A 1999 Transient resonance structure in electron tunneling through water *J. Chem. Phys.* **111** 7558–66

[7] Mott N F and Massey H S W 1933 *The Theory of Atomic Collisions* 1st edn (Oxford: Oxford University Press)
Mott N F and Massey H S W 1965 *The Theory of Atomic Collisions* 3rd edn (Oxford: Oxford University Press)
[8] Goldberger M L and Watson K M 1964 *Collision Theory* (New York: Wiley)
[9] Newton R G 1982 *Scattering Theory of Waves and Particles* (New York: Springer)
[10] Gaspard P and Rice S A 1989 Exact quantization of the scattering from a classically chaotic repellor *J. Chem. Phys.* **90** 2255–62
[11] Gaspard P, Alonso D, Okuda T and Nakamura K 1994 Chaotic scattering on C_{4v} four-disc billiards: semiclassical and exact quantum theories *Phys. Rev.* E **50** 2591–6
[12] Morse P M and Feshbach H 1953 *Methods of Theoretical Physics* (New York: McGraw-Hill)
[13] Arfken G 1985 *Mathematical Methods for Physicists* (San Diego, CA: Academic)
[14] Sloan I H 1968 The numerical evaluation of principal-value integrals *J. Comput. Phys.* **3** 332–3
[15] Davis P J and Rabinowitz P 1984 *Methods of Numerical Integration* (Orlando: Academic)
[16] Ericson T 1960 Fluctuations of nuclear cross sections in the 'continuum' region *Phys. Rev. Lett.* **5** 430–1
[17] Ericson T 1963 A theory of fluctuations in nuclear cross sections *Ann. Phys., NY* **23** 390–414
[18] Brink D M and Stephen R O 1963 Widths of fluctuations in nuclear cross sections *Phys. Lett.* **5** 77–9
[19] Żakowicz W 2003 Classical properties of quantum scattering *J. Phys. A: Math. Gen.* **36** 4445–64